



Article

Investigating the Storm Surge and Flooding in Shenzhen City, China

Peng Bai ^{1,2}, Liangchao Wu ³, Zhoujie Chen ⁴, Jianjun Xu ^{5,6,*}, Bo Li ^{1,2} and Peiliang Li ⁷

¹ Donghai Laboratory, Zhoushan 316021, China; pengbai@zjou.edu.cn (P.B.); acelib@zjou.edu.cn (B.L.)

² Marine Science and Technology College, Zhejiang Ocean University, Zhoushan 316022, China

³ Zhoushan Natural Resource Surveying and Mapping Design Center, Zhoushan 316000, China; wgayaya@163.com

⁴ Zhoushan Natural Resources and Planning Bureau, Zhoushan 316021, China; dingyaowg@163.com

⁵ Shenzhen Institute, Guangdong Ocean University, Shenzhen 518117, China

⁶ South China Sea Institute of Marine Meteorology, College of Ocean and Meteorology, Guangdong Ocean University, Zhanjiang 524088, China

⁷ Hainan Institute, Zhejiang University, Sanya 572025, China; lipeiliang@zju.edu.cn

* Correspondence: jxu@gdou.edu.cn

Abstract: Tropical cyclones affecting Shenzhen city have shown a remarkable tendency to increase in both intensity and quantity, highlighting the urgency of accurate forecasts of storm surges and flooding for effective planning and mitigation. Utilizing satellite and field observations together with the advanced high-resolution baroclinic wave–current model (SCHISM), a comprehensive investigation aimed at storm surge and flooding in Shenzhen was conducted. Statistical work of historical tropical cyclones revealed that Shenzhen was most vulnerable to cyclones propagating from the southeast toward the northwest and passing Shenzhen down the Pearl River Estuary. Thus, a representative, i.e., super typhoon Hato (2017), was selected for further study. Validations of numerical results suggested satisfactory model performance in mapping the wave, tide, and surge processes. Remarkable differences in spatiotemporal distribution and intensity of storm surge and flooding were found along the Shenzhen coast, which was dominated by the propagation of far-field surge and tidal waves, cooperation between wind direction and coastline orientation, estuary morphology, and the land terrain. Intervention of wave–current interaction improved the simulation of the surge and flooding and triggered an earlier occurrence time of the maximum surge in specific areas. The Pearl River discharge significantly elevated the sea level height inside the estuary and contributed to a more severe surge. Given the extremely complicated river networks and huge freshwater flux of Pearl River and the increasing trend of concurrent heavy precipitation of tropical cyclones, future investigations on compound flooding were suggested.

Keywords: storm surge; flooding; wave–current interaction; typhoon Hato; Pearl River Estuary; SCHISM



Citation: Bai, P.; Wu, L.; Chen, Z.; Xu, J.; Li, B.; Li, P. Investigating the Storm Surge and Flooding in Shenzhen City, China. *Remote Sens.* **2023**, *15*, 5002. <https://doi.org/10.3390/rs15205002>

Academic Editor: Domenico Calcaterra

Received: 30 August 2023

Revised: 28 September 2023

Accepted: 16 October 2023

Published: 18 October 2023



Copyright: © 2023 by the authors. Licensee MDPI, Basel, Switzerland. This article is an open access article distributed under the terms and conditions of the Creative Commons Attribution (CC BY) license (<https://creativecommons.org/licenses/by/4.0/>).

1. Introduction

Storm surge refers to the phenomenon of an abnormal sudden rise or a sudden drop in the sea surface caused by strong atmospheric disturbances such as typhoons or cold spells. If a storm surge occurs during the high period of an astronomical tide, the water level will rise sharply, and even the sea water will rush up to the land, resulting in flooding disasters. Storm surges and flooding disasters often occur simultaneously and lead to devastating damage, including, but not limited to, serious loss of life and property in coastal areas [1,2].

The dynamics of storm surges and flooding have attracted extensive attention. Topographic characteristics are demonstrated as the key factor affecting the spatial and temporal distribution of storm surges and flooding. In the deep sea, the storm surge generally changes gently over a broad area; thus, the model with a relatively rough resolution can

also obtain accurate simulation results [3–7], but in the nearshore or estuaries, a storm surge often characterizes significant spatial differences in a narrow range due to the complex changes of coastline and topography, and only high-resolution models simulate reasonable results [8–11]. Moreover, under the combined action of human activities and natural evolution, the coastline morphology and coastal water depth keep changing with time, which will cause spatiotemporal adjustments in storm surges and flooding [6,12].

A storm surge in the nearshore area can be regarded as the superposition of two parts: one is the locally generated surge by the local strong wind and low pressure; another is the surge that forms in the far field along the typhoon track and propagates to the local area. The propagation of far-field surge is affected by the local terrain and coastline, which often cause significant surge differences between the upper and lower reaches of bays or estuaries. For instance, Guo et al. [8] reported that under the bell-shaped terrain of Hangzhou Bay, the intensity of a far-field storm surge doubled as it came from the mouth area to the top region. In most cases, the storm surges in coastal waters are mainly dominated by far-field storm surges, while the contribution of a local storm surge is small [13]. However, as revealed by Jones and Davies [9], the contribution of a local storm surge can equally match that of a far-field storm surge in the eastern Irish Sea. In fact, except for the topography, the development of a local storm surge is also largely dependent on the direction of the typhoon wind [14].

Under a strong weather process (e.g., typhoon or cold spell), intense ocean waves and currents will develop, and therefore, remarkable two-way interactions between them occur. Wave–current interaction is well known to considerably modify the intensity of storm surges and flooding. When waves enter the shallow area, the wave height increases and the wave slope steepens and finally breaks up to produce a shoreward mass flux and changes the sea surface height, i.e., wave setup and wave setdown [15]. Beardsley et al. [11] pointed out that the maximum surge height increased by 8 cm and became closer to the observation after considering wave–current interaction; meanwhile, the simulated inundation area expanded significantly. A statistical investigation of wave setup triggered by historical cyclones revealed that the magnitude of the largest wave setup along most parts of the eastern United States coast was 0.1 m [16]. Wave force plays a decisive role in the momentum balance under the forcing of a typhoon, and a simulation of a storm surge can be considerably improved when wave force is introduced using the radiation stress scheme or the vortex force scheme [17]. Moreover, in some extreme cases, the contribution of wave setup can even reach up to 40% of the total surge height [18]. Hence, wave–current interaction is a critical factor for high prediction skill of storm surge and flooding.

In the context of global warming, sea level rise will also modify the storm surge and flooding [4,19]. Scholars estimated that the average sea level rise in 100 years will be between 0.22 m and 1.90 m [20–23]. Sea level rise may adjust the relative contribution of near-field and far-field atmospheric forcing to storm surges, thereby changing the spatial distribution of maximum storm surges [24]. In addition, the resolution of the computational grid largely determines the ability of the model to describe the real terrain during the numerical simulation of storm surges and flooding, which in turn affects the simulation accuracy of storm surges and flooding [11].

Shenzhen city is located to the north of the South China Sea, which extends from the east shore of the Pearl River Estuary to the north coasts of Dapeng Bay and Daya Bay (Figure 1a–c). Shenzhen is one of China’s three major national financial centers and one of the four major central cities in the Guangdong–Hong Kong–Macao Greater Bay Area. However, statistical results reveal that there are 5.83 tropical cyclones affecting the Greater Bay Area per year on average, and 46.62% of them reach the level of typhoon; moreover, the frequency of strong typhoons impacting the Greater Bay Area has increased significantly in the past decade [25]. Therefore, Shenzhen is also a vulnerable disaster-bearing body under the severe threat of storm surges and flooding.

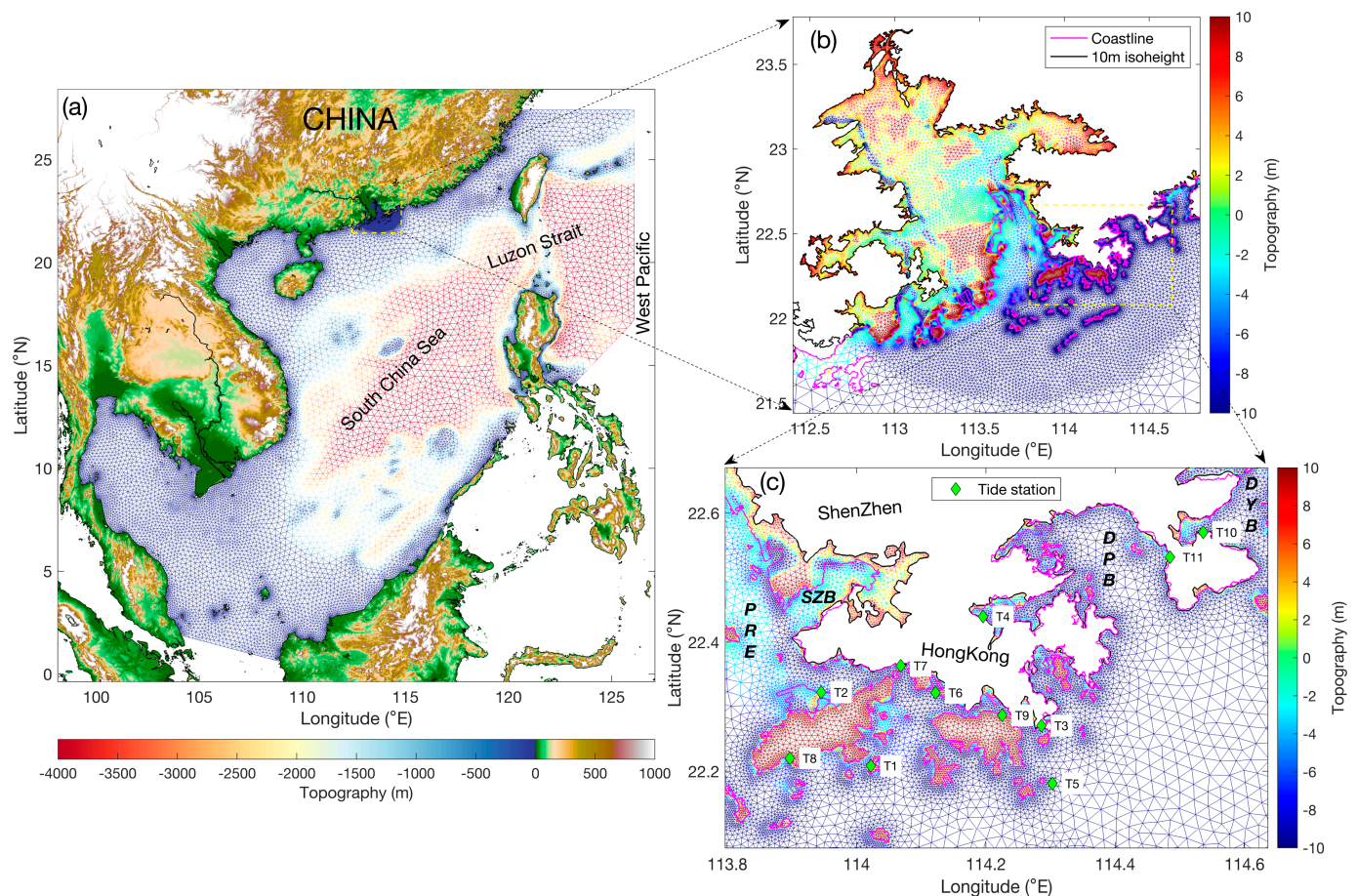


Figure 1. (a) Topography and SCHISM computational grid of the study domain. (b) Zoom-in of the grid in Pearl River Estuary, purple and black lines mark off the coastline and 10 m isoheight, respectively. (c) Zoom-in of the grid around Shenzhen city; green diamonds show locations of tide stations; PRE, SZB, DPB, and DYB are abbreviations for Pearl River Estuary, Shenzhen Bay, Dapeng Bay, and Daya Bay, respectively.

To date, there are few specific investigations aimed at storm surges and flooding in the coastal area of Shenzhen, but most of them are mainly based on barotropic numerical models and ignore the flooding process, and some of them do not even consider the contribution of wave–current interaction. To achieve a better understanding of the storm surge and flooding in Shenzhen, a comprehensive study based on satellite and field observations together with an advanced high-resolution baroclinic wave–current model has been conducted. The remaining parts of this paper are organized as follows: Section 2 illustrates the data and method employed in this work; Section 3 mainly documents a storm surge and flooding event in Shenzhen from various aspects; Section 4 discusses the controlling factors of storm surge and flooding in the study domain; and finally, Section 5 presents a brief conclusion of this work.

2. Materials and Methods

2.1. Remote-Sensed Significant Wave Height

Satellite-observed significant wave height (H_s) is a powerful and widely used material for studying the ocean environment [26–29]. In this work, we employed the Level-2 along-track H_s products provided by the NOAA Laboratory for Satellite Altimetry (LSA) to investigate the typhoon waves as well as examine the model performance in simulating ocean waves. Moreover, H_s from satellites Jason-2, Sentinel-3A, CryoSat-2, and SARAL through August 2017 with a 2 km+ spatial resolution were all used to enrich the data quantities.

Detailed introduction and data access are available at <https://coastwatch.noaa.gov/cwn/products/along-track-significant-wave-height-wind-speed-and-sea-level-anomaly-multiple-altimeters.html> (accessed on 16 January 2023).

2.2. Typhoon Data

Located in the tropical region, storm surges and flooding in Shenzhen are mainly triggered by typhoons. To understand the characteristics of historical typhoons that affected Shenzhen, we utilized the version 4 typhoon product from the International Best Track Archive for Climate Stewardship (IBTrACS) project, which is the most complete global collection of tropical cyclones available. IBTrACS Version 4 merges recent and historical tropical cyclone data from multiple agencies; their extensive usage in typhoon-associated studies has proven their high quality. These data can be acquired from the National Centers for Environmental Information (<https://www.ncei.noaa.gov/products/international-best-track-archive>, accessed on 10 January 2023).

2.3. Tide Station Data

The evolution of storm surge and flooding processes can be directly reflected in the variation of sea level height (SLH). The SLH data observed at 11 tide stations (Figure 1c) were used to validate the model and discuss the storm surge and flooding processes in Shenzhen. The hourly SLH from 15 April to 25 April 2015 at stations T1–T9 was acquired from the Hong Kong Observatory (<https://www.hko.gov.hk/en/index.html>, accessed on 25 April 2015), while the SLH from 21 August to 25 August 2017 with a 10 min interval at stations T10 and T11 was provided by coastal marine stations Dongshan and Nanao, respectively.

2.4. Numerical Modeling

In addition to multi-source observations, we have implemented the Semi-implicit Cross-scale Hydroscience Integrated System Model (SCHISM) [30] for the South China Sea (Figure 1a). SCHISM is a seamless creek-to-ocean 3D hydrodynamic model with accurate, robust, and efficient semi-implicit time stepping; in the horizontal dimension, it supports hybrid finite-element/finite-volume methods on hybrid triangular–quadrangular unstructured grids (i.e., SCHISM enables users to conduct variable-resolution modeling); while in the vertical direction, a highly flexible terrain-following vertical gridding system (LSC²) [31] is applied. There have been worldwide successful applications of SCHISM since its release; further information on SCHISM can be found at <http://ccrm.vims.edu/schismweb/> (accessed on 16 January 2022).

A set of wet–dry triangular grids covering the entire South China Sea with local refinement in the Pearl River Estuary and its adjacent seas was designed (Figure 1a,b). In the modeling domain, there are 116,414 triangular elements and 62,209 nodes, making the horizontal resolution in the Shenzhen coastal area reach up to 180 m. Moreover, the grid extends from sea to the land by 10 m isoheight to fully resolve the flooding process in the Pearl River Estuary and its adjacent areas (Figure 1b). Taking advantage of SCHISM's polymorphism, the number of vertical layers varies depending on local water depth, with a maximum of 57 layers in the deepest region. Topography of the grid was obtained by merging the SRTM15 + V2.1 product (<https://doi.org/10.5069/G92R3PT9>, accessed on 25 July 2022) together with local electronic nautical charts. SRTM15 + V2.1 is a broadly used global bathymetry and topography grid with a spatial sampling interval of 15 arc seconds, of which the bathymetry originates from the combination of shipboard soundings and depths predicted using satellite altimetry.

Tidal harmonic constants of M_2 , S_2 , N_2 , K_2 , K_1 , O_1 , P_1 , Q_1 , M_f , and M_m tidal constituents interpolated from FES2014 were adopted as tidal forcing. Initial and boundary conditions (when needed) were both interpolated from the GLOBAL_MULTIYEAR_PHY_001_030 product provided by Copernicus Marine Service Information (CMEMS); this is a global reanalysis displayed on a standard regular grid at $1/12^\circ$ (~8 km) and on 50 standard levels.

Air–sea heat, momentum, and freshwater fluxes (when needed) were all derived from the CFSv2 6-hourly reanalyzed product (<https://rda.ucar.edu/datasets/ds094.0/>, accessed on 20 July 2022).

To examine the model reliability in simulating the tidal dynamics and explore the roles of wave–current interaction and river discharge playing in storm surge and flooding, four numerical experiments named “Barotropic”, “Uncoupled”, “Coupled”, and “Coupled + River” were conducted, of which the detailed configurations are listed in Table 1. Note that the feedback from current to wave was turned off to focus on the contribution of wave–current interaction to storm surge.

Table 1. Model configurations of all numerical experiments.

Configuration Case Name	Barotropic	Uncoupled	Coupled	Coupled + River
Initial condition	Motionless; constant temperature and salinity	CMEMS	CMEMS	CMEMS
Boundary condition	N/A	CMEMS	CMEMS	CMEMS
Tidal forcing	FES2014	FES2014	FES2014	FES2014
Air–sea fluxes	N/A	CFSv2	CFSv2	CFSv2
Wave–current interaction	N/A	Off	On	On
Pearl River discharge	N/A	Off	Off	On
Modeling period	20140301–20140430	20170701–20170831	20170701–20170831	20170701–20170831

2.5. Model Skill Assessment

To objectively examine the performance of the model in reproducing local hydrodynamics, a widely-used skill assessment parameter [26,32–36] is defined as the following:

$$SKILL = 1 - \frac{\sum_{i=1}^N (\eta_{\text{model}} - \eta_{\text{observed}})^2}{\sum_{i=1}^N (|\eta_{\text{model}} - \eta_{\text{observed}}| + |\eta_{\text{observed}} - \eta_{\text{observed}}|)^2},$$

where η_{model} and η_{observed} are the simulated and observed values, respectively; the overbar denotes the temporal average; and $SKILL = 1$ means perfect simulation, while $SKILL = 0$ indicates the worst simulation.

Meanwhile, the root mean square error (RMSE), which indicates the average distance between the modeled and observed values, was used:

$$RMSE = \sqrt{\sum_{i=1}^N (\eta_{\text{model}} - \eta_{\text{observed}})^2 / N}.$$

To further measure the linear dependence between the modeled and observed values, the correlation coefficient (CC) is defined as the following:

$$CC = \frac{1}{N-1} \sum_{i=1}^N \left(\frac{\eta_{\text{model}} - \mu_{\text{model}}}{\sigma_{\text{model}}} \right) \left(\frac{\eta_{\text{observed}} - \mu_{\text{observed}}}{\sigma_{\text{observed}}} \right),$$

where μ_{model} and σ_{model} are the mean and standard deviation of modeled values, while μ_{observed} and σ_{observed} are the mean and standard deviation of observed values.

3. Results

3.1. Tropical Cyclones Affecting Shenzhen

For a specific coastal region, the typhoon track is a critical factor in determining the intensity and spatiotemporal distribution of storm surges [24]. Based on the IBTrACS Version 4 data, we analyzed the tropical cyclones passing the South China Sea during 1842–2019. Tropical cyclones that transited through the circle area, of which the center is located in the middle of Pearl River Estuary mouth with a radius of 200 km, are defined as

cyclones potentially triggering storm surges and flooding in Shenzhen. Taking the track as a criterion, tropical cyclones that affected Shenzhen can be sorted into 15 categories: SE-NW-DOWN, SE-NW-UP, SE-NW-MIDDLE, SW-NE-DOWN, SW-NE-UP, SW-NE-MIDDLE, S-N-LEFT, S-N-RIGHT, E-W-DOWN, E-W-MIDDLE, E-W-UP, W-E-DOWN, NE-SW-DOWN, NE-SW-UP, and OTHERS (for instance, SE-NW-DOWN means the cyclone propagates from the southeast toward the northwest and passing Shenzhen down the Pearl River Estuary; the type OTHERS indicates the track of the cyclone is very irregular and hardly to categorize).

Figure 2a,b show the statistics of tropical cyclones with different tracks and the representative track of each kind, respectively. As revealed, tropical cyclones of the SE-NW-DOWN category are absolutely dominant and account for 47.2% of the total numbers. Therefore, super typhoon Hato (storm ID: 2017232N19130; Figures 2b and 3a), one of the SE-NW-DOWN category cyclones, was selected as a representative to explore storm surge and flooding in Shenzhen.

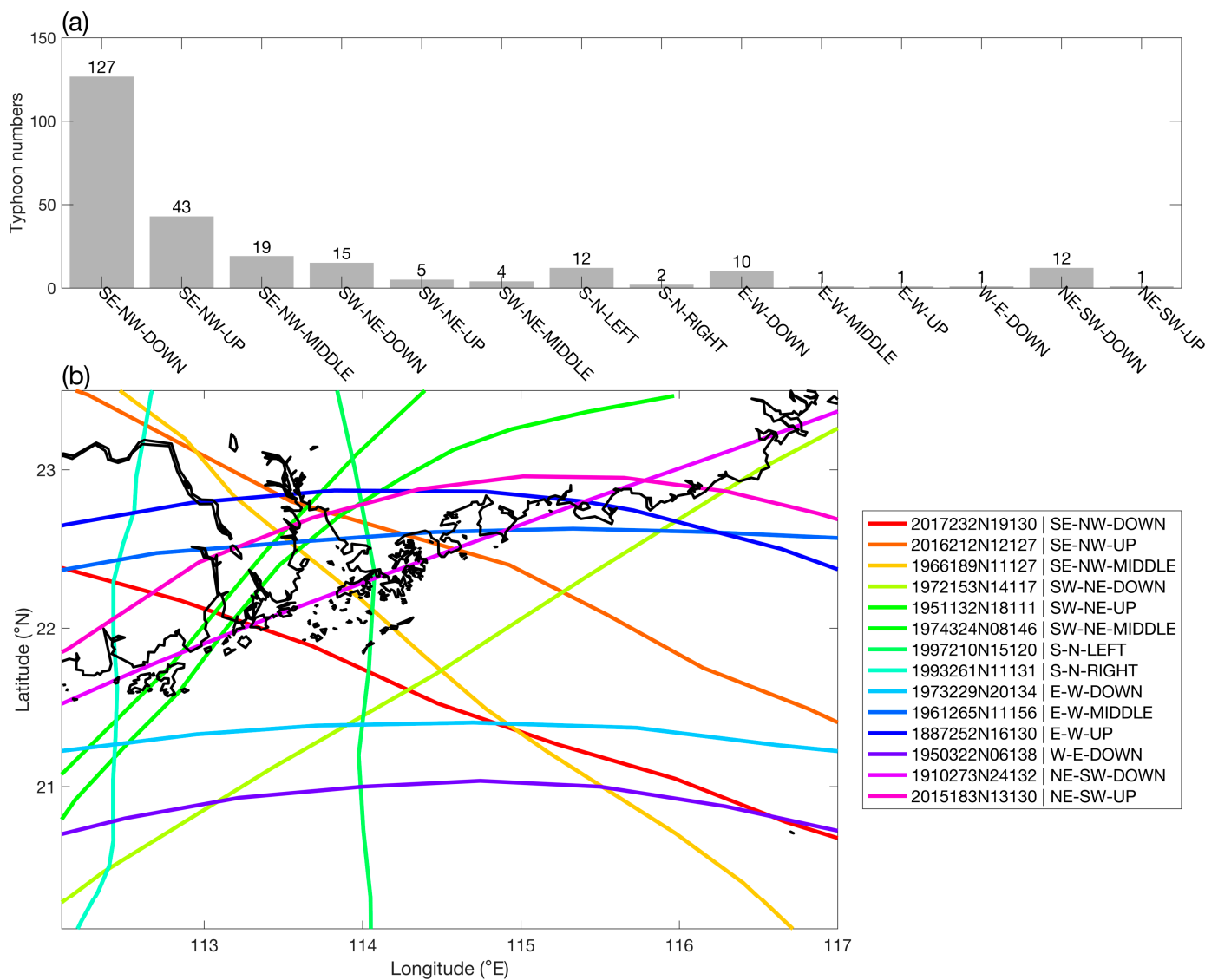


Figure 2. (a) Statistics of tropical cyclones striking Pearl River Estuary with different tracks. (b) Representative cyclone track of each kind.

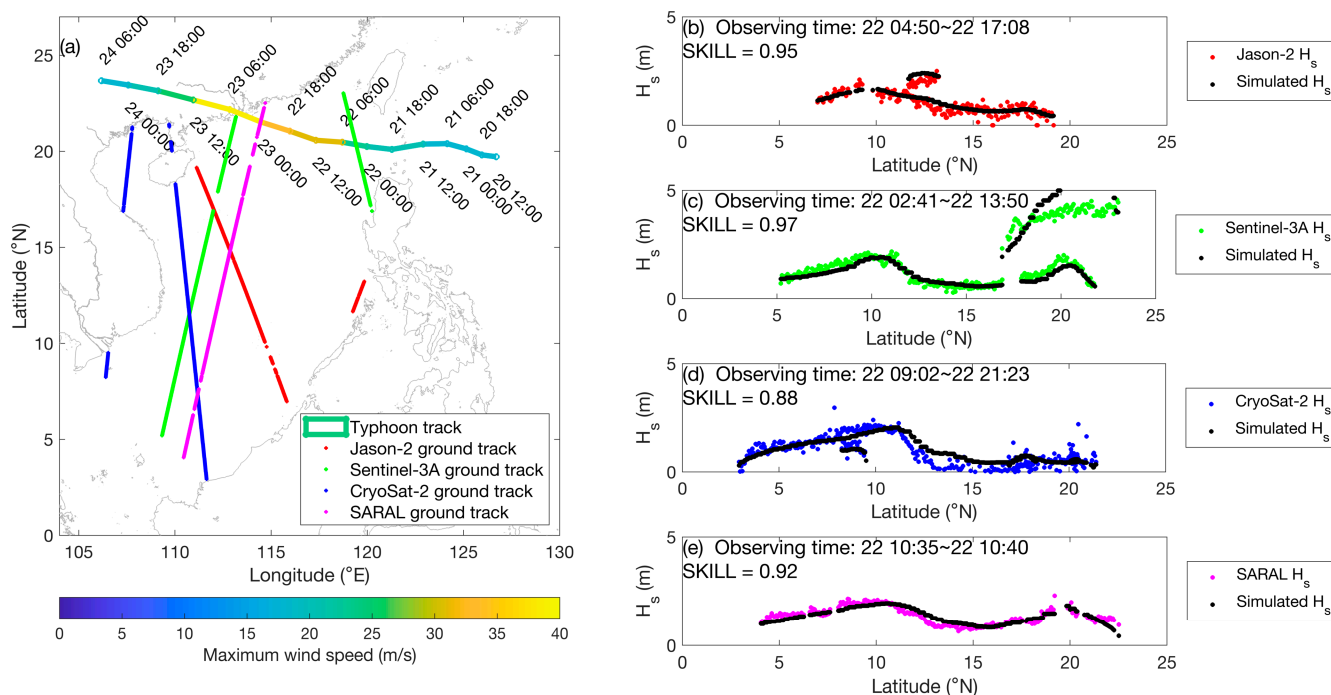


Figure 3. (a) Ground tracks of Jason-2, Sentinel-3A, CryoSat-2, and SARAL during 22–23 August 2017 and track of super typhoon Hato (2017). (b–e) Comparisons of significant wave height between the simulations (data from Uncoupled case) and observations using different satellites along those ground tracks shown in (a).

The track and intensity of Hato are displayed in Figure 3a; it developed over the northwest Pacific and entered the South China Sea on 22 August through the Luzon Strait. Later, the maximum wind speed increased from 33 m/s to 52 m/s in one day as Hato propagated toward the northwest. Finally, the eye of Hato landed at the southwest of Pearl River Estuary with a 45 m/s gust at 0400 UTC on 23 August 2017, leading to immeasurable damage and becoming one of the most intense and severe typhoons striking China ever.

3.2. Validation of Wave Simulation

The significant wave height (H_s) is one of the most representative characteristics of waves. As Hato entered South China, the wave field would remarkably adjust in response to typhoon force. We first examined the simulated H_s during 22–23 August 2017, i.e., the typhoon forcing period. Satellites Jason-2, Sentinel-3A, CryoSat-2, and SARAL were found to be observed during this period; their ground tracks are shown in Figure 3a using different colors. The along-track comparisons of observed and modeled H_s are displayed in Figure 3b–e, respectively. Generally, the modeled H_s agree well with the observations both in intensity and spatial distribution along all tracks. The model skill originated from the comparisons based on Jason-2, Sentinel-3A, CryoSat-2, and SARAL H_s observations are 0.95, 0.97, 0.88, and 0.92, respectively, proving a satisfying model ability in mapping the wave dynamics under typhoons.

Further, H_s observations with Jason-2, Jason-3, Sentinel-3A, CryoSat-2, and SARAL through August 2017 were utilized to conduct an enhanced validation of the model. Figure 4a shows the ground tracks of five altimeters, while the comparison results are presented in Figure 4b. The model skill is 0.92 over a total number of 36,253 point-to-point contrasts. Moreover, the RMSE and CC between the modeled and observed H_s are 0.34 m and 0.86, respectively. Thus, as Figures 3 and 4 revealed, the model can accurately simulate the waves not only under normal weather conditions but also applicable to the typhoon process.

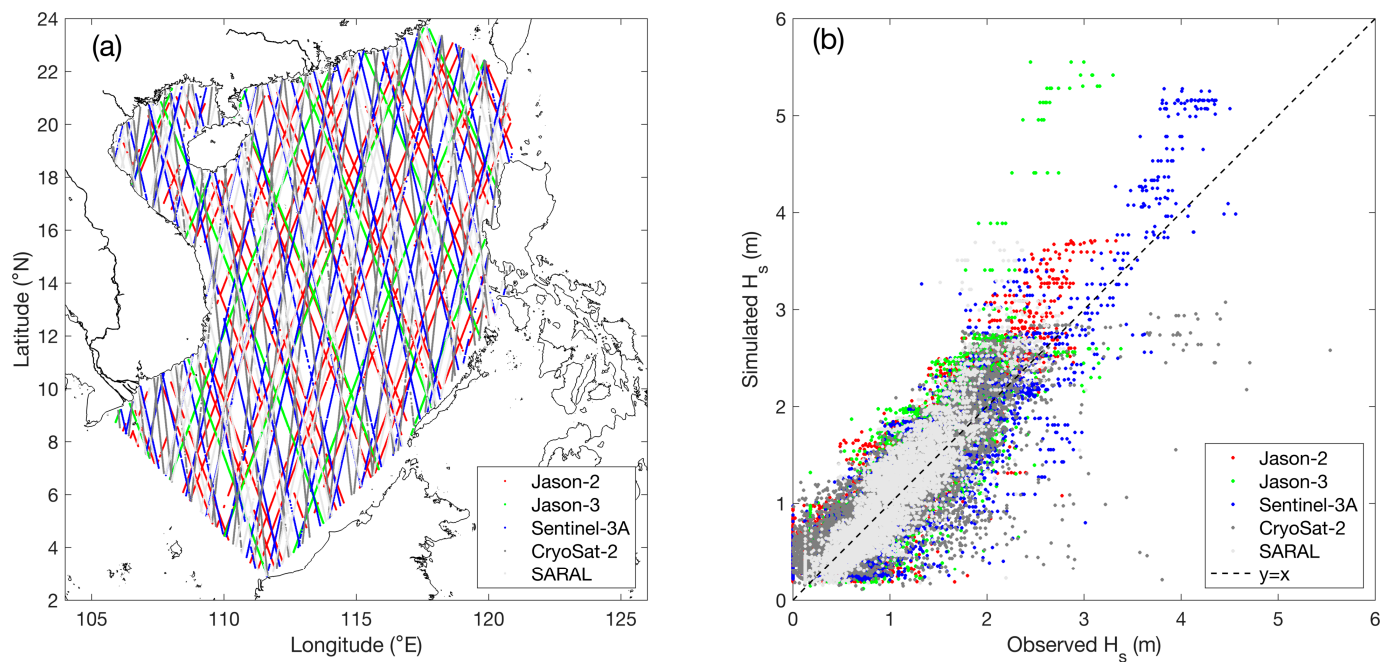


Figure 4. (a) Ground tracks of Jason-2, Jason-3, Sentinel-3A, CryoSat-2, and SARAL in the study domain during 1–31 August 2017. (b) Comparisons between observed and modeled (data from Uncoupled case) significant wave height of different satellites.

3.3. Validation of Tide Simulation

The sea level height (SLH) in nearshore areas is mainly dominated by the tides. Thus, the reliable tidal performance of the model is necessary for accurate storm surge and flooding simulation. Comparisons between SLH observations and simulations (results from the barotropic case) at tide stations T1–T9 (Figure 1c) are shown in Figure 5a–i, respectively. As displayed, the model can reasonably present the magnitude as well as the phase of periodically fluctuating SLH; the model skills at tide stations T1–T9 are 0.96, 0.94, 0.95, 0.93, 0.92, 0.96, 0.96, 0.96, and 0.94, respectively, showing satisfying tidal performance.

3.4. Validation of Surge Simulation

Tide stations T10 and T11 (Figure 1c) completely recorded the variation of SLH throughout the strike of Hato, and these data were used to examine the model performance in the surge process. As Figure 6 displayed, the model (Couple + River case) reasonably hindcasts the abnormal high SLH (i.e., storm surge) by Hato: the maximum observed and simulated SLH are 3.40 m (3.89 m) and 3.39 m (3.83 m), respectively at station T10 (T11), producing a 0.01 m (0.06 m) model error. Therefore, the reliable model performance is qualified for further explorations.

Further, tidal harmonic analysis was conducted at stations T1–T11 using the SLH modeled using the barotropic case. Thus, the astronomic tides during the studied period can be calculated based on existing tidal harmonic constants. Then, the surge height can be obtained through deducting the SLH induced by astronomic tides from the total SLH, and the time series of surge height at stations T10 and T11 modeled using different numerical cases during the passage of typhoon Hato are displayed in Figure 6c,d, respectively. As revealed, the surge first appeared at 00:00 on 21 August and gradually strengthened until 16:00 on 22 August, then a sharp increase occurred, and the surge height reached its peak around 03:00 on 23 August. Following the peak, the surge height mainly kept lowering till 00:00 on 24 August. Note that there were fluctuations in both the rising and lowering phases.

There are little differences among the surges modeled using various numerical cases during the period 12 h before or after the peak surge. At stations T10 and T11, the maximum

surge modeled with the Uncoupled case is 0.01–0.06 m lower than that using the Coupled case. Meanwhile, there is a minor difference between the Coupled and Coupled + River cases (Figure 6c,d). Given that the maximum SLH produced with Coupled + River is slightly lower than the observations (Figure 6a,b), it could be inferred that wave–current interaction improves the model skill for the surge at stations T10 and T11, but the contribution of the Pearl River discharge is insignificant there, and this will be further discussed in Section 4.

3.5. Storm Surge along Shenzhen Coast

There are five coastal districts, Dapeng, Yantian, Futian, Nanshan, and Baoan, in Shenzhen city (Figure 7k); they extend from the east shore of Pearl River Estuary to the north of Dapeng Bay and Daya Bay with significant separation by Hong Kong in the middle. To understand the spatiotemporal differences of storm surge along the Shenzhen coast, 10 representative coastal stations (S1–S10) are selected, and their locations are shown in Figure 7k, while the surge height modeled with different numerical cases at stations S1–S10 are shown in Figure 7a–j, respectively.

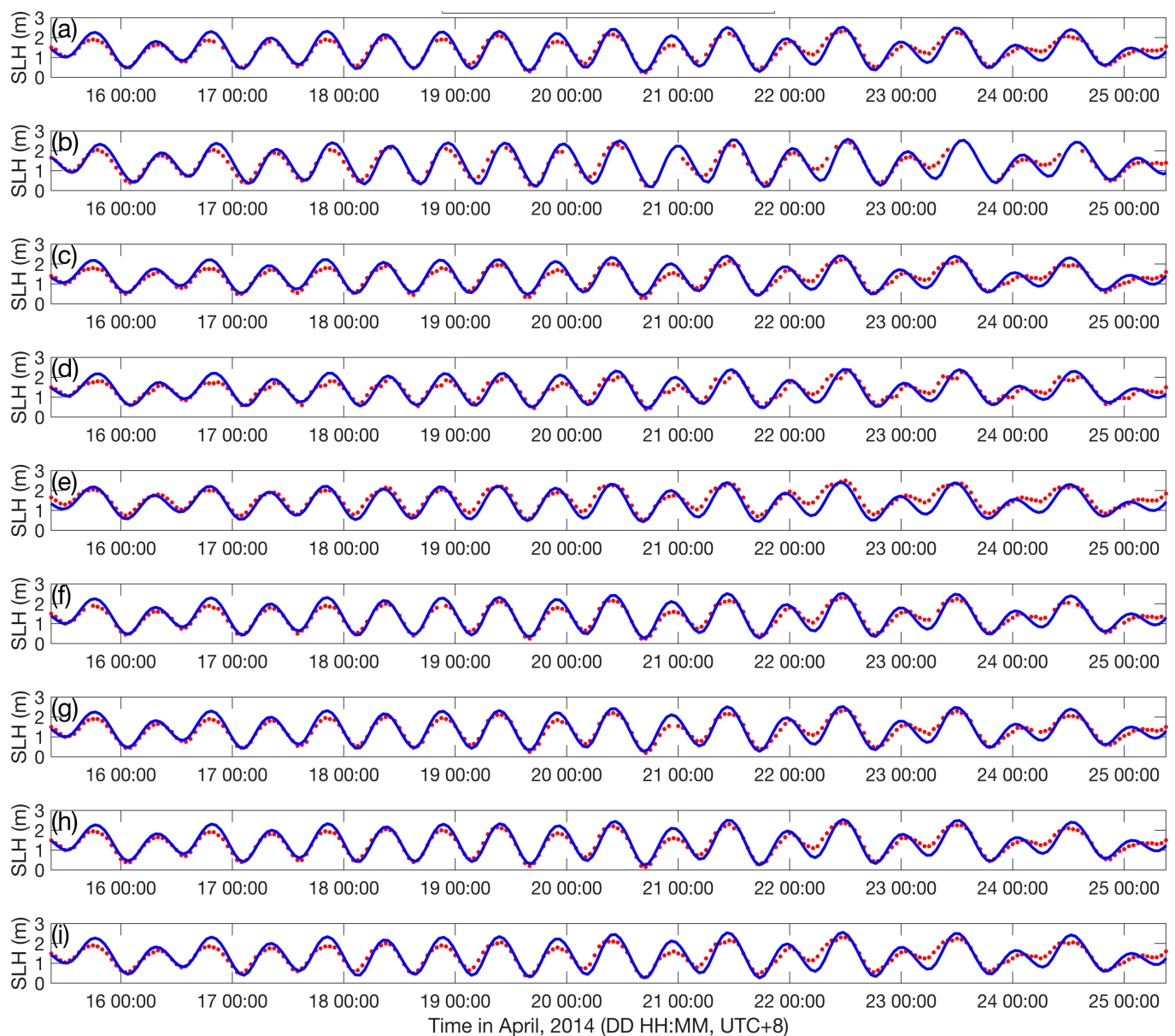


Figure 5. (a–i) show the comparisons between observed sea level height and modeled result at tide stations T1–T9 shown in Figure 1c, successively.

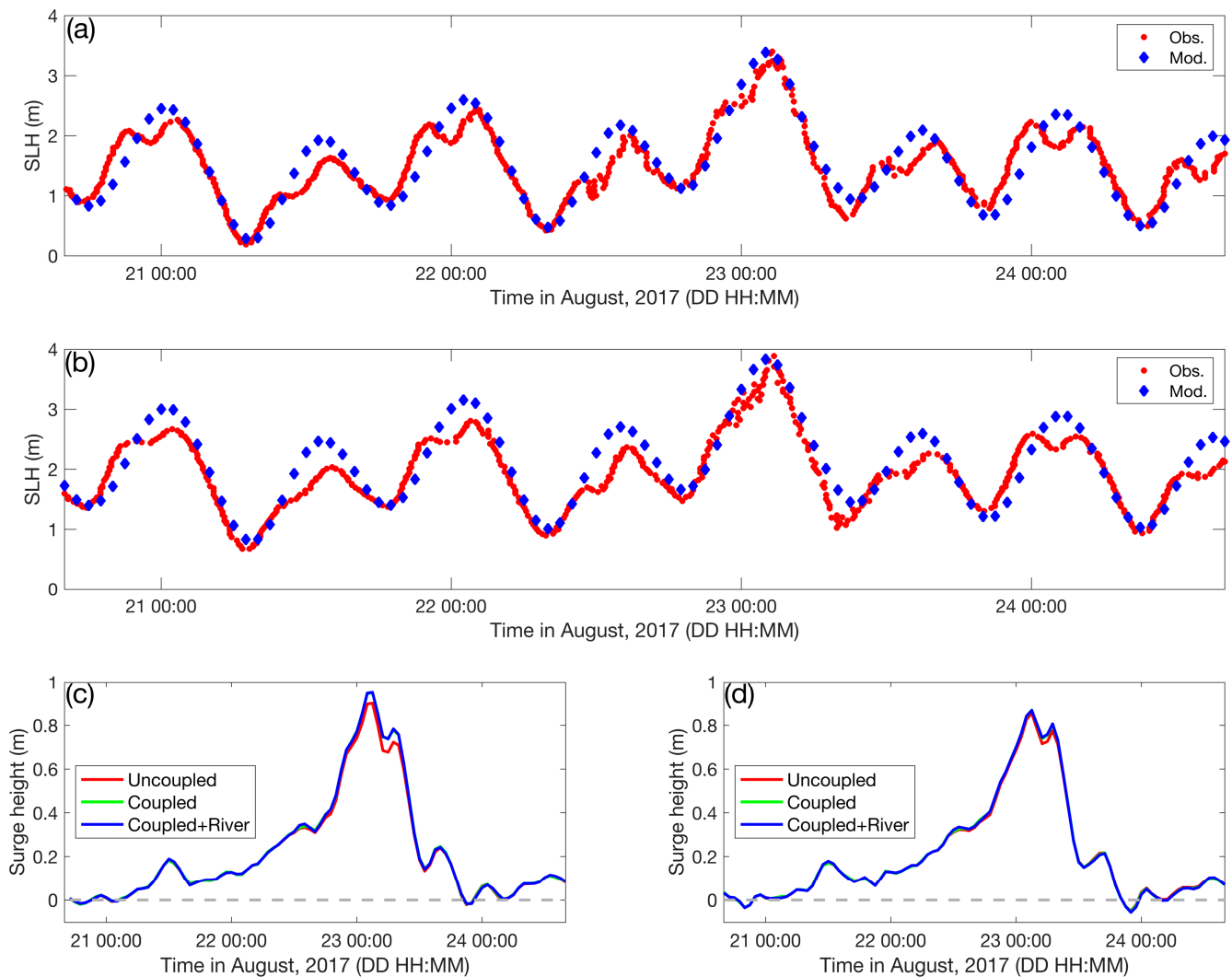


Figure 6. (a,b) show the comparisons between observed sea level height and modeled result (Coupled + River case) at tide stations T10 and T11 shown in Figure 1c during the strike of super typhoon Hato (2017), respectively. (c,d) display time series of surge height simulated using different numerical cases at stations T10 and T11, respectively.

From the perspective of time, as shown in Figure 7, the maximum storm surge outside the Pearl River Estuary occurred about 7 h earlier than that inside the estuary. Meanwhile, the occurrence time of a maximum storm surge is gradually postponed as it comes from the middle estuary to the upper estuary.

From the perspective of space, in the stations adjacent to Dapeng Bay and Daya Bay (S1–S6), the storm surge at stations on the windward side (S1, S2, and S6) was significantly higher than those stations on the leeward side (S3–S5) during the strike of super typhoon Hato. Meanwhile, the maximum surge height inside the Pearl River Estuary was generally larger compared with the surge along the coast of the Dapeng and Yantian districts.

Further, Figure 7 also suggests that the maximum surge height increased by 0.02–0.08 m after taking wave–current interaction into consideration; outside the Pearl River Estuary, wave–current interaction contributed to an average of 0.05 m surge over six stations (S1–S6); however, only an average of 0.02 m surge was triggered via wave–current interaction over stations (S7–S10) inside the estuary. In addition, the maximum surge height was 0.01–0.13 m higher when adding the discharge of Pearl River into the model; on average, 0.11 m and 0.01 m increases in surge height were found inside and outside the Pearl River Estuary, respectively.

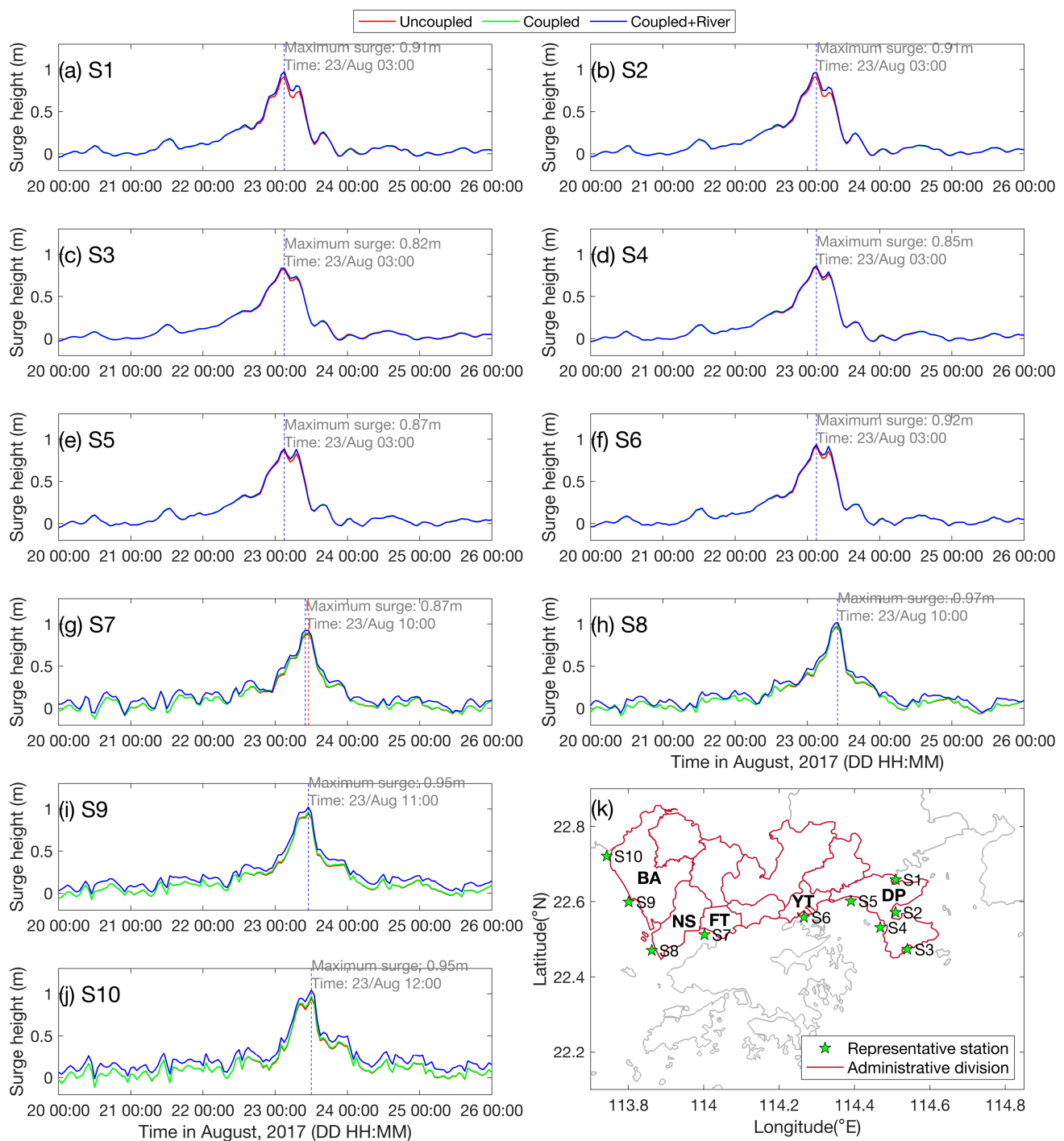


Figure 7. (a–j) show the time series of surge height at representative stations S1–S10 along the coastal districts of Shenzhen city; locations of representative stations are shown in (k). Abbreviations DP, YT, FT, NS, and BA denote Dapeng, Yantian, Futian, Nanshan, and Baoan coastal districts of Shenzhen city, respectively.

3.6. Flooding along the Shenzhen Coast

Based on the Coupled + River case, we then explored the spatiotemporal characteristics of flooding in the coastal zone of Shenzhen. The maximum flooding area, its occurrence time, and the flood depth of Dapeng, Yantian, Futian, Nanshan, and Baoan districts are displayed in Figure 8. In the districts inside Pearl River Estuary, the occurrence time of maximum flooding falls behind those outside the estuary, indicating that the surge signal

propagated from east toward west under the forcing of Hato. Note that the occurrence time of maximum flooding was not the same as that of maximum surge height; this is easy to understand: maximum surge height does not equal the highest SLH.

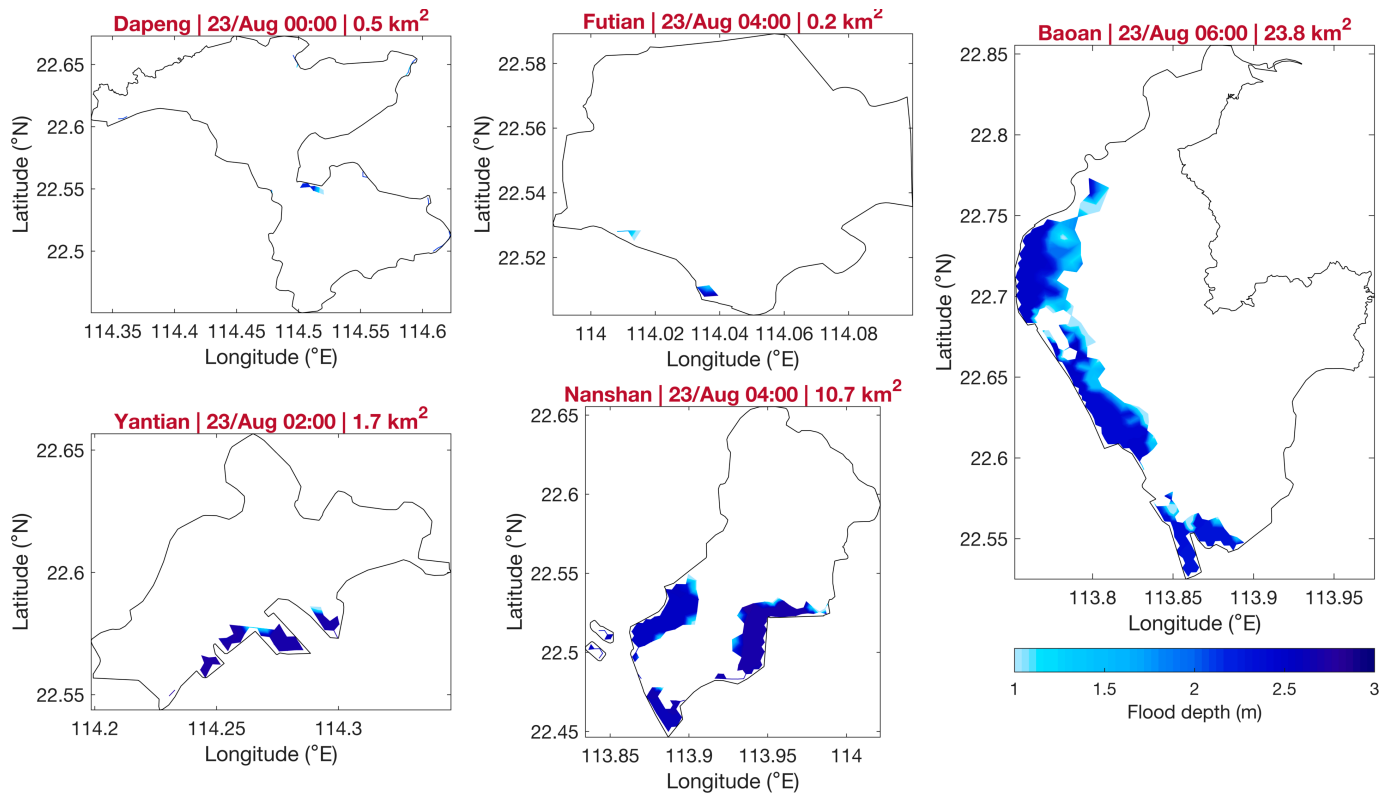


Figure 8. Distribution of inundation area and flood depth in the coastal districts of Shenzhen city: Dapeng, Yantian, Futian, Nanshan, and Baoan, respectively. Note the mapping scale is not unified.

The inundation area of districts inside the Pearl River Estuary was generally broader than those outside the estuary. Meanwhile, the most and second severe flooding occurred in Baoan and Nanshan, with inundation areas of 23.8 and 10.7 km², respectively. Compared with Baoan and Nanshan, the flooding in Futian, Dapeng, and Yantian was much weaker, and the inundation area was about one order of magnitude smaller than the former ones.

4. Discussion

4.1. Occurrence Time of Maximum Surge and Flooding

During the strike of Hato, Figure 7 reveals a significant difference in the occurrence time of maximum surge in different areas of Shenzhen. On one hand, Hato propagated along an SE-NW track (Figure 3a); thus, a far-field surge signal would first arrive at the eastern shore of Shenzhen and then enter the Pearl River Estuary to reach the western shore of the city. On the other hand, a typhoon wind field usually characterizes a spiral structure, as shown in Figure 9. Shoreward winds, in favor of the development of local surge, also first appeared in the eastern parts of Shenzhen and dominated the districts adjacent to Pearl River Estuary later. The cooperation between wind direction and coastline orientation plays a vital role in the occurrence time of maximum surge in different areas, and that is why previous investigations emphasized the importance of typhoon tracks on storm surge [24]. Moreover, the low sea surface air pressure at the typhoon center is also a key contributor to storm surge because it will help the SLH to rise. As typhoon Hato propagated from southeast to northwest, the far-field surge signal generated by low air pressure in the open sea would also propagate toward the coast and first arrive at the eastern shore of Shenzhen for a shorter distance, which is also in favor of the earlier occurrence time of maximum surge there compared with the areas inside the Pearl River Estuary.

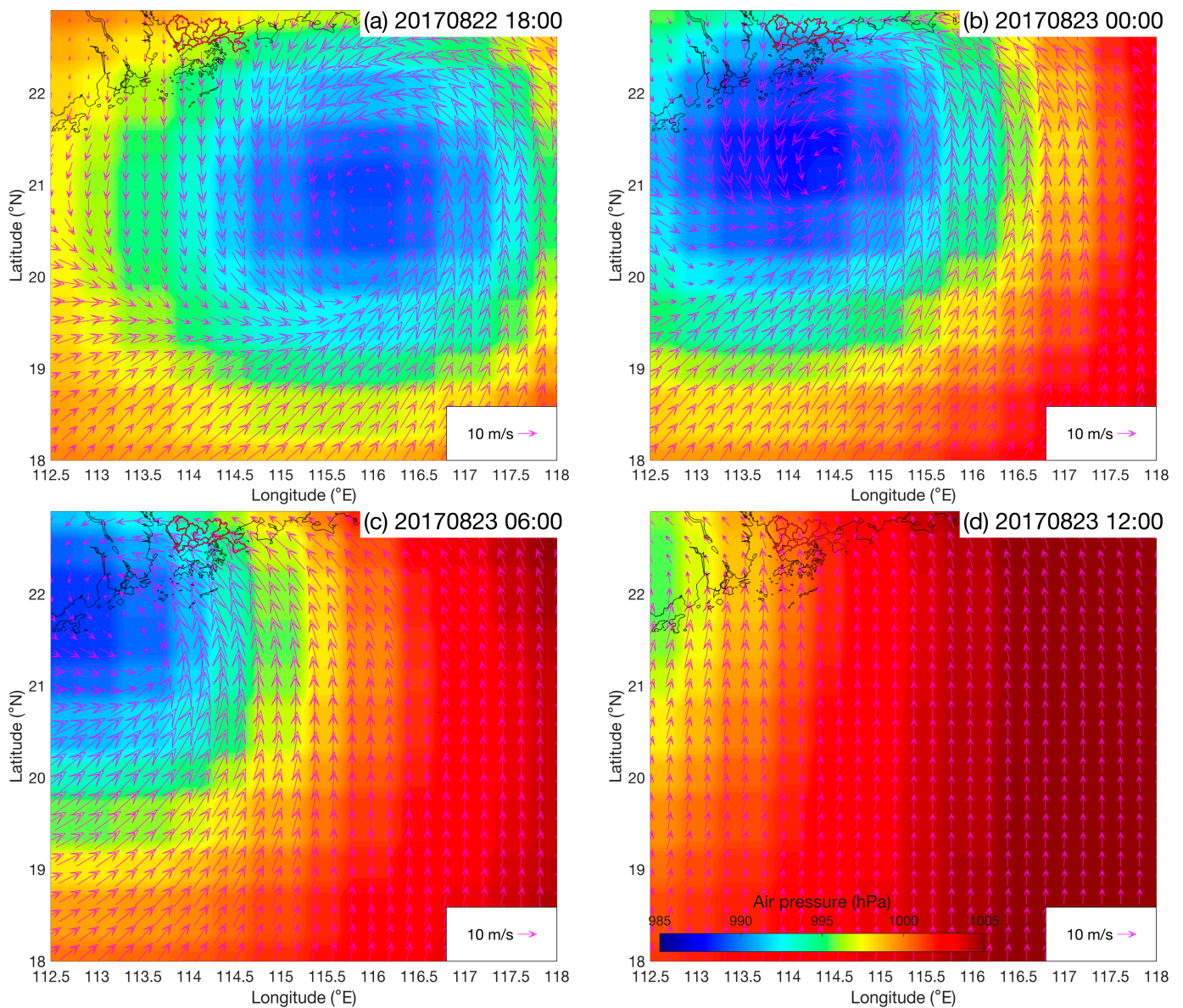


Figure 9. (a–d) show 10 m wind vectors superposed on sea surface air pressure (data originated from CFSv2 product) at 18:00 22 August, 00:00 23 August, 06:00 23 August, and 12:00 23 August 2017, respectively. Administration division borders of Shenzhen are marked in dusky red.

The occurrence time of maximum flooding was also gradually postponed from the east coast of Shenzhen to the west (Figure 8). One reason is that, as discussed above, the maximum surge occurred earlier in the northern Dapeng Bay and Daya Bay than in the eastern Pearl River Estuary. However, maximum surge is not necessarily in sync with maximum SLH, and maximum SLH depends on the cooperation between storm surge and astronomic tides.

The tidal system in the Pearl River Estuary is mainly driven by tidal energy from the West Pacific through the Luzon Strait: both diurnal and semi-diurnal tidal waves propagate toward the southwest as they enter the South China Sea, passing by the eastern shore of Shenzhen and then arriving at the estuary. Figure 10a–d display spatial distribution of tidal phases of M_2 , S_2 , K_1 , and O_1 constituents, respectively. As revealed, the tidal phases of M_2 , S_2 , K_1 , and O_1 constituents along the western coast of Shenzhen approximately lag behind those along the eastern shore by 55° , 80° , 25° , and 35° (i.e., 1.83 h, 2.76 h, 1.66 h, and 2.51 h

time lag in respective high tide), respectively. Thus, the spatial difference of the tidal phase is another reason for the varying occurrence time of maximum flooding.

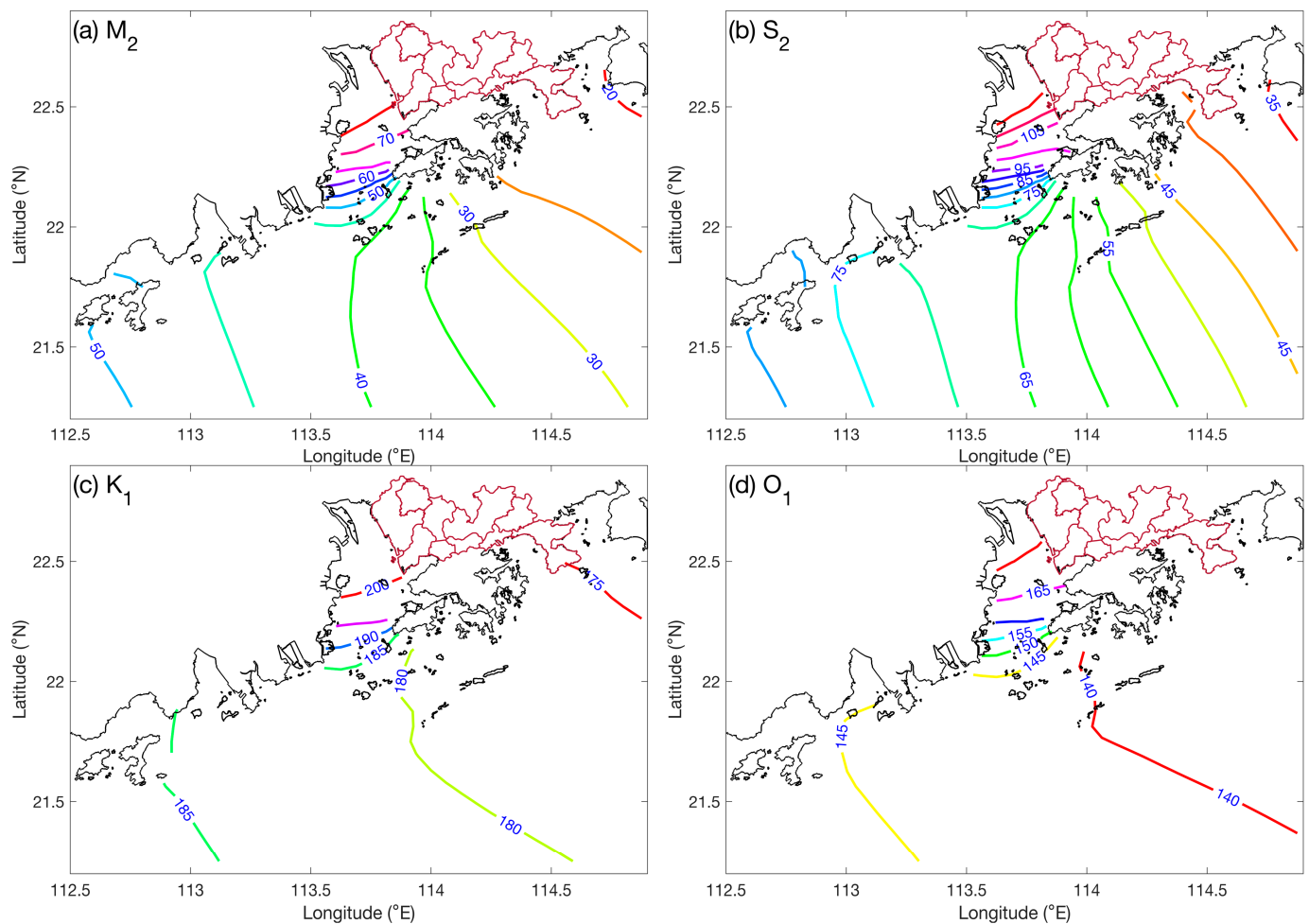


Figure 10. (a–d) show tidal phases of M_2 , S_2 , K_1 , and O_1 constituents in the study domain, respectively. Administration division borders of Shenzhen are marked in dusky red.

4.2. Role of Topography

Figure 11 shows the altitude of five coastal districts of Shenzhen. As Figures 8 and 10 revealed, the distributions of maximum flooding are in good agreement with the low-lying areas in these coastal districts. Under the strong forcing of Hato, flooding in Shenzhen barely broke through the 5 m altitude line. For the Baoan district, there are broad, low-lying coastal areas, which explains why the maximum flooding occurred there to a large extent. Another reason is that Baoan is located in the top region of the bell-shaped Pearl River Estuary, where the stormwater from the open sea will be easily accumulated by the shrinking terrain and, in turn, produce higher SLH. Results suggested that Baoan, followed by Nanshan and Yantian, should enhance the embankment work aimed at those low-lying zones.

4.3. Role of Wave–Current Interaction and River Discharge

The increase in surge height via wave–current interaction outside Pearl River Estuary is larger than that outside the estuary, which was reported in Section 3.5. The main reason is that waves inside the estuary are weaker than those outside the estuary (not shown) due to the shallow and semi-enclosed topography, and thus the wave-setup process is much weaker. Table 2 lists the observed and modeled maximum SLH at stations T10 and T11;

as suggested, consideration of wave–current interaction improves model performance at both stations.

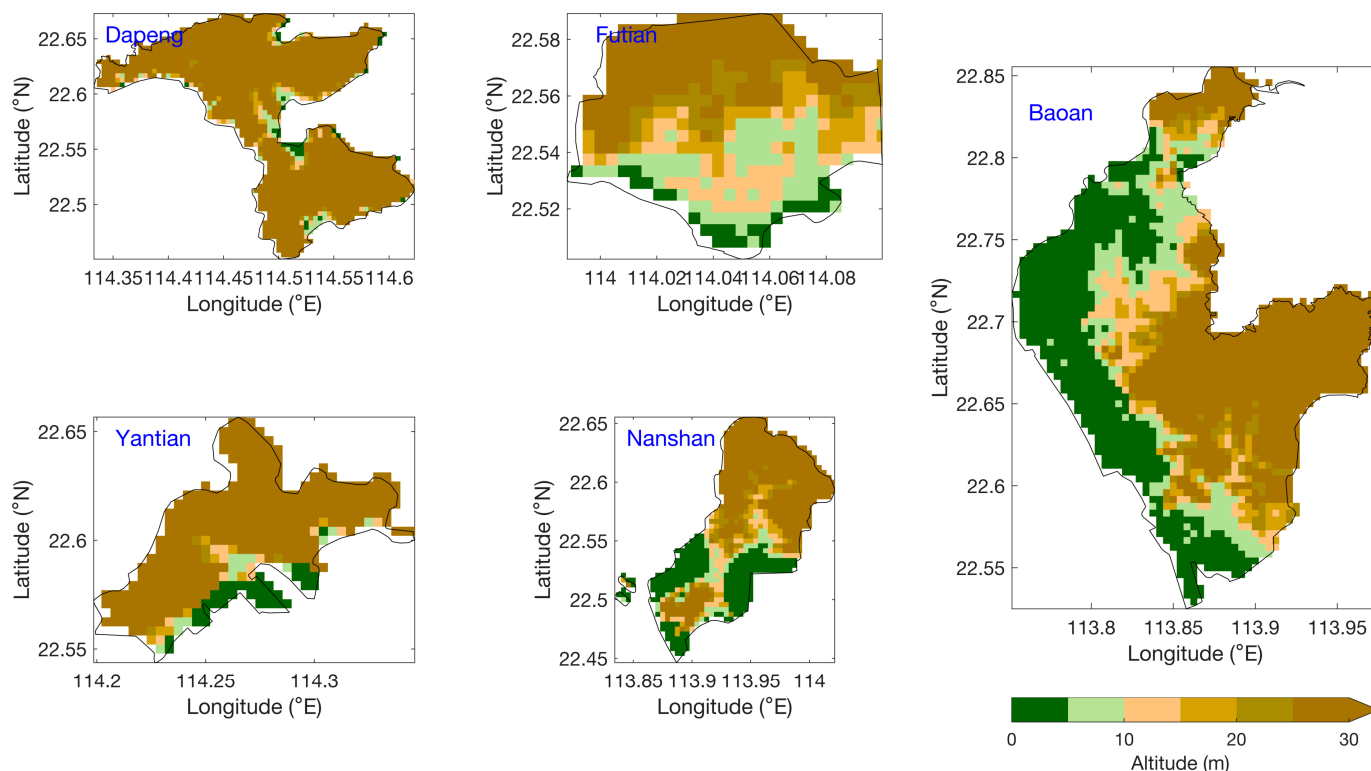


Figure 11. Altitude of the coastal districts of Shenzhen city: Dapeng, Yantian, Futian, Nanshan, and Baoan, respectively.

Table 2. Observed and modeled maximum SLH at stations T10 and T11 (unit: m); values in brackets are simulating errors.

Station Case	Observation	Uncoupled	Coupled	Coupled + River
T10	3.40	3.34 (0.06)	3.39 (0.01)	3.39 (0.01)
T11	3.89	3.82 (0.07)	3.83 (0.06)	3.83 (0.06)

Another interesting point lies in the different occurrence times of maximum surge triggered via wave–current interaction. Figure 7g reveals that the maximum surge occurred 1 h earlier at station S7 as wave–current interaction was considered. This reminds us of the importance of using the wave–current coupled model in forecasting storm surge and flooding because the accurate prediction of maximum surge and flooding occurrence time is crucial for formulating disaster response plans and, thus, for saving lives and properties.

In terms of river discharge, Pearl River is the second largest river in China, with an annual average flux of $1 \times 10^4 \text{ m}^3/\text{s}$, which is a dominant factor for the ocean biogeochemical environment in the estuary and its adjacent seas. A strong salinity front is one of the most typical phenomena triggered by continuously incoming fresh water (Figure 12a). In Section 3.5, a significant increase (0.11 m) in surge height by the river discharge was found inside the estuary. Therefore, we examined the SLH difference between the Coupled and Coupled + River numerical cases before the strike of Hato, and the result is displayed in Figure 12b. The intervention of Pearl River discharge elevated SLH by ~ 0.1 m in the estuary but ~ 0 m in the far field, which well explains the spatial difference of river discharge’s contribution (Figures 7 and 12b).

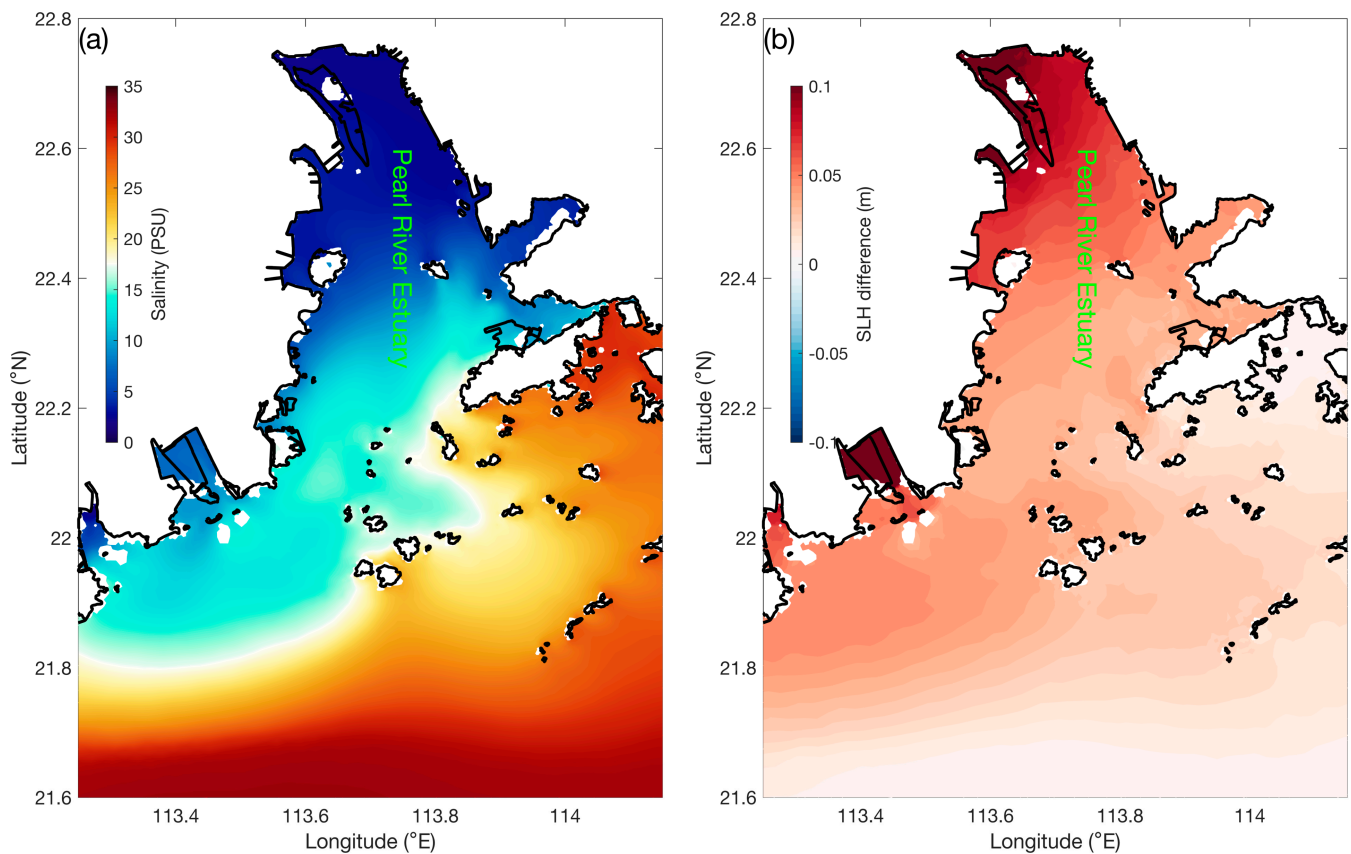


Figure 12. (a) Distribution of sea surface salinity simulated with case Coupled+River in Pearl River Estuary. (b) Difference of sea level height between cases Coupled+River and Coupled (former minus latter) before the strike of super typhoon Hato (2017).

5. Conclusions

Recent tropical cyclones affecting Shenzhen have shown a remarkable tendency to increase in both intensity and quantity [25], highlighting the urgency of accurate forecasts of storm surges and flooding for effective planning and mitigation. Hence, we have conducted a comprehensive study based on satellite and field observations together with an advanced high-resolution baroclinic wave–current model to gain a better understanding of the storm surge and flooding in Shenzhen; the major new findings are as follows:

- (1) Classification of historical tropical cyclones reveals that Shenzhen city is most vulnerable to cyclones propagating from the southeast toward the northwest and passing Shenzhen down the Pearl River Estuary (i.e., type SE-NW-DOWN);
- (2) Propagation of far-field surge and tidal waves, cooperation between wind direction and coastline orientation, estuary morphology, and land terrain together dominate the spatiotemporal distribution and intensity of storm surge and flooding in Shenzhen;
- (3) We highlight the importance of wave–current interaction and river discharge in the forecast of storm surge and flooding in Shenzhen: wave–current interaction improves the simulation of storm surge and may modify the occurrence time of maximum surge height, while river discharge can elevate the background SLH, particularly in the inner estuary.

Actually, there are three types of flooding processes threatening coastal areas: storm surge and flooding, precipitation-driven flooding, and river flooding. Their compound effects have been proven to play a vital role in estuaries [37,38]. Given the extremely complicated river networks and huge freshwater flux of Pearl River and the increasing trend of concurrent heavy precipitation of tropical cyclones [39], compound flooding should be investigated in further investigations.

Author Contributions: Conceptualization, P.B. and J.X.; methodology, P.B. and P.L.; software, P.B.; validation, B.L. and P.L.; formal analysis, P.B. and J.X.; investigation, P.B.; resources, J.X. and B.L.; data curation, L.W. and Z.C.; writing—original draft preparation, P.B. and J.X.; writing—review and editing, P.B.; visualization, P.B.; supervision, J.X. and P.L.; project administration, J.X. and B.L.; funding acquisition, B.L., J.X., P.B. and P.L. All authors have read and agreed to the published version of the manuscript.

Funding: This study was funded by the Shenzhen Science and Technology Program (Grant Number JCYJ20210324131810029), the Science Foundation of Donghai Laboratory (Grant Number DH-2022KF0208), the National Natural Science Foundation of China (Grant Number 42106017), the Guangdong Basic and Applied Basic Research Foundation (Grant Number 2020A1515110516), the Special Fund for Technology Development of Zhanjiang City (Grant Number 2020A01008), the Hainan Provincial Joint Project of Sanya Yazhou Bay Science and Technology City (Grant Number 2021CXLH0020).

Data Availability Statement: Data employed in this study can be acquired by contacting the corresponding author at jxu@gdou.edu.cn (J.X.).

Acknowledgments: The authors appreciate the helpful discussions with members of the Marine Process and Equipment Group from the Ocean University of China. The numerical simulation was conducted on the HPC of Beijing Super Cloud Computing Center.

Conflicts of Interest: The authors declare no conflict of interest.

References

1. Fritz, H.M.; Blount, C.; Sokoloski, R.; Singleton, J.; Fuggle, A.; McAdoo, B.G.; Moore, A.; Grass, C.; Tate, B. Hurricane Katrina Storm Surge Distribution and Field Observations on the Mississippi Barrier Islands. *Estuar. Coast. Shelf Sci.* **2007**, *74*, 12–20. [[CrossRef](#)]
2. Needham, H.F.; Keim, B.D.; Sathiaraj, D. A Review of Tropical Cyclone-generated Storm Surges: Global Data Sources, Observations, and Impacts. *Rev. Geophys.* **2015**, *53*, 545–591. [[CrossRef](#)]
3. Lowe, J.A.; Gregory, J.M.; Flather, R.A. Changes in the Occurrence of Storm Surges around the United Kingdom under a Future Climate Scenario Using a Dynamic Storm Surge Model Driven by the Hadley Centre Climate Models. *Clim. Dyn.* **2001**, *18*, 179–188. [[CrossRef](#)]
4. Horsburgh, K.J.; Wilson, C. Tide-Surge Interaction and Its Role in the Distribution of Surge Residuals in the North Sea. *J. Geophys. Res.* **2007**, *112*, C08003. [[CrossRef](#)]
5. Olbert, A.I.; Hartnett, M. Storms and Surges in Irish Coastal Waters. *Ocean Model.* **2010**, *34*, 50–62. [[CrossRef](#)]
6. Haigh, I.D.; MacPherson, L.R.; Mason, M.S.; Wijeratne, E.M.S.; Pattiaratchi, C.B.; Crompton, R.P.; George, S. Estimating Present Day Extreme Water Level Exceedance Probabilities around the Coastline of Australia: Tropical Cyclone-Induced Storm Surges. *Clim. Dyn.* **2014**, *42*, 139–157. [[CrossRef](#)]
7. Pasquali, D.; Di Risio, M.; De Girolamo, P. A Simplified Real Time Method to Forecast Semi-Enclosed Basins Storm Surge. *Estuar. Coast. Shelf Sci.* **2015**, *165*, 61–69. [[CrossRef](#)]
8. Guo, Y.; Zhang, J.; Zhang, L.; Shen, Y. Computational investigation of typhoon-induced storm surge in Hangzhou Bay, China. *Estuar. Coast. Shelf Sci.* **2009**, *85*, 530–536. [[CrossRef](#)]
9. Jones, J.E.; Davies, A.M. Storm Surge Computations for the Irish Sea Using a Three-Dimensional Numerical Model Including Wave–Current Interaction. *Cont. Shelf Res.* **1998**, *18*, 201–251. [[CrossRef](#)]
10. Dietrich, J.C.; Bunya, S.; Westerink, J.J.; Ebersole, B.A.; Smith, J.; Atkinson, J.H.; Jensen, R.E.; Resio, D.T.; Luettich, R.A.; Dawson, C.; et al. A High-Resolution Coupled Riverine Flow, Tide, Wind, Wind Wave, and Storm Surge Model for Southern Louisiana and Mississippi. Part II: Synoptic Description and Analysis of Hurricanes Katrina and Rita. *Mon. Weather Rev.* **2010**, *138*, 378–404. [[CrossRef](#)]
11. Beardsley, R.C.; Chen, C.; Xu, Q. Coastal Flooding in Scituate (MA): A FVCOM Study of the 27 December 2010 nor’easter. *J. Geophys. Res. Oceans* **2013**, *118*, 6030–6045. [[CrossRef](#)]
12. Zhang, K.; Li, Y.; Liu, H.; Xu, H.; Shen, J. Comparison of Three Methods for Estimating the Sea Level Rise Effect on Storm Surge Flooding. *Clim. Change* **2013**, *118*, 487–500. [[CrossRef](#)]
13. Soontiens, N.; Allen, S.E.; Latornell, D.; Le Souëf, K.; Machuca, I.; Paquin, J.-P.; Lu, Y.; Thompson, K.; Korabel, V. Storm Surges in the Strait of Georgia Simulated with a Regional Model. *Atmos. Ocean* **2016**, *54*, 1–21. [[CrossRef](#)]
14. Shen, J.; Gong, W. Influence of Model Domain Size, Wind Directions and Ekman Transport on Storm Surge Development inside the Chesapeake Bay: A Case Study of Extratropical Cyclone Ernesto, 2006. *J. Mar. Syst.* **2009**, *75*, 198–215. [[CrossRef](#)]
15. Longuet-Higgins, M.S.; Stewart, R.W. Radiation Stress and Mass Transport in Gravity Waves, with Application to ‘surf-Beats’. *J. Fluid. Mech.* **1962**, *13*, 481–504. [[CrossRef](#)]
16. Marsooli, R.; Lin, N. Numerical Modeling of Historical Storm Tides and Waves and Their Interactions Along the U.S. East and Gulf Coasts. *J. Geophys. Res. Oceans* **2018**, *123*, 3844–3874. [[CrossRef](#)]

17. Zhang, C.; Hou, Y.; Li, J. Wave-current interaction during Typhoon Nuri (2008) and Hagupit (2008):an application of the coupled ocean-wave modeling system in the northern South China Sea. *J. Oceanol. Limnol.* **2018**, *36*, 663–675. [[CrossRef](#)]
18. Kim, S.Y.; Yasuda, T.; Mase, H. Wave Set-up in the Storm Surge along Open Coasts during Typhoon Anita. *Coast. Eng.* **2010**, *57*, 631–642. [[CrossRef](#)]
19. Feng, J.; Jiang, W.; Bian, C. Numerical Prediction of Storm Surge in the Qingdao Area Under the Impact of Climate Change. *J. Ocean Univ. China* **2014**, *13*, 539–551. [[CrossRef](#)]
20. Chen, J. The Impact of Sea Level Rise on China's Coastal Areas and Its Disaster Hazard Evaluation. *J. Coast. Res.* **1997**, *13*, 925–930.
21. Rahmstorf, S. A Semi-Empirical Approach to Projecting Future Sea-Level Rise. *Science* **2007**, *315*, 368–370. [[CrossRef](#)] [[PubMed](#)]
22. Vermeer, M.; Rahmstorf, S. Global Sea Level Linked to Global Temperature. *Proc. Natl. Acad. Sci. USA* **2009**, *106*, 21527–21532. [[CrossRef](#)] [[PubMed](#)]
23. Katsman, C.A.; Sterl, A.; Beersma, J.J.; van den Brink, H.W.; Church, J.A.; Hazeleger, W.; Kopp, R.E.; Kroon, D.; Kwadijk, J.; Lammersen, R.; et al. Exploring High-End Scenarios for Local Sea Level Rise to Develop Flood Protection Strategies for a Low-Lying Delta—The Netherlands as an Example. *Clim. Chang.* **2011**, *109*, 617–645. [[CrossRef](#)]
24. Liu, X.; Jiang, W.; Yang, B.; Baugh, J. Numerical Study on Factors Influencing Typhoon-Induced Storm Surge Distribution in Zhanjiang Harbor. *Estuar. Coast. Shelf Sci.* **2018**, *215*, 39–51. [[CrossRef](#)]
25. Ye, R.; Ge, J.; Zhang, W.; Zhao, H. Statistical analysis on impact from tropical cyclone on Guangdong-Hong Kong-Macao Greater Bay Area. *Water Resour. Hydropower Eng.* **2020**, *51*, 37–43. (In Chinese)
26. Yang, J.; Jiang, S.; Wu, J.; Xie, L.; Zhang, S.; Bai, P. Effects of Wave-Current Interaction on the Waves, Cold-Water Mass and Transport of Diluted Water in the Beibu Gulf. *Acta Oceanol. Sin.* **2020**, *39*, 25–40. [[CrossRef](#)]
27. Yao, R.; Shao, W.; Hao, M.; Zuo, J.; Hu, S. The Response of Wave on Sea Surface Temperature in the Context of Global Change. *Remote Sens.* **2023**, *15*, 1948. [[CrossRef](#)]
28. Li, R.; Wu, K.; Zhang, W.; Dong, X.; Lv, L.; Li, S.; Liu, J.; Babanin, A.V. Analysis of the 20-Year Variability of Ocean Wave Hazards in the Northwest Pacific. *Remote Sens.* **2023**, *15*, 2768. [[CrossRef](#)]
29. Jiang, Y.; Rong, Z.; Li, Y.; Li, C.; Meng, X. Toward a High-Resolution Wave Forecasting System for the Changjiang River Estuary. *Remote Sens.* **2023**, *15*, 3581. [[CrossRef](#)]
30. Zhang, Y.J.; Ye, F.; Stanev, E.V.; Grashorn, S. Seamless Cross-Scale Modeling with SCHISM. *Ocean Model.* **2016**, *102*, 64–81. [[CrossRef](#)]
31. Zhang, Y.J.; Ateljevich, E.; Yu, H.-C.; Wu, C.H.; Yu, J.C.S. A New Vertical Coordinate System for a 3D Unstructured-Grid Model. *Ocean Model.* **2015**, *85*, 16–31. [[CrossRef](#)]
32. Willmott, C.J. On the validation of models. *Phys. Geogr.* **1981**, *2*, 184–194. [[CrossRef](#)]
33. Warner, J.C.; Geyer, W.R.; Lerczak, J.A. Numerical Modeling of an Estuary: A Comprehensive Skill Assessment. *J. Geophys. Res.* **2005**, *110*, C05001. [[CrossRef](#)]
34. Zhong, L.; Li, M. Tidal Energy Fluxes and Dissipation in the Chesapeake Bay. *Cont. Shelf Res.* **2006**, *26*, 752–770. [[CrossRef](#)]
35. Pan, J.; Gu, Y.; Wang, D. Observations and Numerical Modeling of the Pearl River Plume in Summer Season. *J. Geophys. Res. Oceans* **2014**, *119*, 2480–2500. [[CrossRef](#)]
36. Bai, P.; Gu, Y.; Li, P.; Wu, K. Tidal Energy Budget in the Zhujiang (Pearl River) Estuary. *Acta Oceanol. Sin.* **2016**, *35*, 54–65. [[CrossRef](#)]
37. Ye, F.; Zhang, Y.J.; Yu, H.; Sun, W.; Moghimi, S.; Myers, E.; Nunez, K.; Zhang, R.; Wang, H.V.; Roland, A.; et al. Simulating Storm Surge and Compound Flooding Events with a Creek-to-Ocean Model: Importance of Baroclinic Effects. *Ocean Model.* **2020**, *145*, 101526. [[CrossRef](#)]
38. Huang, W.; Ye, F.; Zhang, Y.J.; Park, K.; Du, J.; Moghimi, S.; Myers, E.; Pe'eri, S.; Calzada, J.R.; Yu, H.C.; et al. Compounding Factors for Extreme Flooding around Galveston Bay during Hurricane Harvey. *Ocean Model.* **2021**, *158*, 101735. [[CrossRef](#)]
39. Pfahl, S.; O'Gorman, P.A.; Fischer, E.M. Understanding the Regional Pattern of Projected Future Changes in Extreme Precipitation. *Nat. Clim. Chang.* **2017**, *7*, 423–427. [[CrossRef](#)]

Disclaimer/Publisher's Note: The statements, opinions and data contained in all publications are solely those of the individual author(s) and contributor(s) and not of MDPI and/or the editor(s). MDPI and/or the editor(s) disclaim responsibility for any injury to people or property resulting from any ideas, methods, instructions or products referred to in the content.